Journal of Materials Chemistry C

ROYAL SOCIETY OF CHEMISTRY

PAPER

View Article Online
View Journal | View Issue

Cite this: J. Mater. Chem. C, 2022, 10, 8407

Ferroelectric $Hf_{0.5}Zr_{0.5}O_2$ films on $SrTiO_3(111)$†

Tingfeng Song,‡ Saúl Estandía,‡ Nico Dix, Jaume Gàzquez, Martí Gich, Ignasi Fina * and Florencio Sánchez *

Received 11th March 2022,
Accepted 1st May 2022

DOI: 10.1039/d2tc00996j

rsc.li/materials-c

Ferroelectric HfO_2 epitaxial films are of interest for determining intrinsic properties and for prototyping devices. Epitaxial (111)-oriented orthorhombic $Hf_{0.5}Zr_{0.5}O_2$ films grown on $La_{0.67}Sr_{0.33}MnO_3/SrTiO_3(001)$ are already being actively investigated. Presently, we have explored the use of $SrTiO_3(111)$ substrates. We show that the orthorhombic phase is stabilized by tilted epitaxy, and the orientation of orthorhombic crystallites is different from that of equivalent films on $SrTiO_3(001)$. The measured remanent polarization of above 14 μC cm^{-2} agrees well with the expected value considering the crystal orientation, the fraction of the ferroelectric phase in the film, and the predicted polarization for ferroelectric HfO_2. High endurance and retention are also measured.

1. Introduction

The discovery[1] of ferroelectricity in a metastable orthorhombic phase ($Pca2_1$ space group) of Si-doped HfO_2 has generated huge interest.[2–7] The ferroelectric phase has also been stabilized in HfO_2 doped with other atoms.[7,8] The ferroelectric properties of HfO_2 have been investigated mainly in polycrystalline films, although there is increasing interest in epitaxial films after the demonstration of epitaxial stabilization on yttria-stabilized zirconia[9] and perovskite[10–12] single crystalline substrates. Epitaxial orthorhombic films present excellent ferroelectric properties[13] and they are more robust against polarization – endurance and endurance – retention dilemmas than polycrystalline films.[14,15] Moreover, the ferroelectricity of ultrathin films, 2–4 nm thick, has been confirmed by direct electrical measurements of epitaxial samples.[14,16] These results have been achieved mostly in epitaxial films deposited on (001)-oriented $La_{0.67}Sr_{0.33}MnO_3$ (LSMO) electrodes. The polarization is null or very low when other conducting perovskite oxides such as $SrRuO_3$ and $LaNiO_3$ are used as bottom electrodes.[17] Very recently, the epitaxial growth of orthorhombic $Hf_{0.5}Zr_{0.5}O_2$ (HZO) on (110)-oriented LSMO electrodes has also been reported.[18,19] $Hf_{0.5}Zr_{0.5}O_2$ (HZO) films or other HfO_2 doped compounds grown on LSMO(001) or LSMO(110) are (111) oriented, while the ferroelectric dipoles are oriented along the [001] direction.

The epitaxial stabilization of the ferroelectric phase on LSMO(111) electrodes would be of high interest as it can lead to a different orientation of the ferroelectric dipoles in the film. Moreover, it could pave the way towards the epitaxial integration of ferroelectric HfO_2 on other substrates with a 3-fold symmetry surface. Aiming to determine if the ferroelectric phase of HfO_2 can be stabilized on LSMO(111), we have deposited HZO films on $LSMO(111)/SrTiO_3(111)$. We show that the orthorhombic phase is epitaxially stabilized, but it is not (111) oriented. Detailed X-ray diffraction (XRD) and scanning transmission electron microscopy (STEM) characterization studies reveal the existence of three families of orthorhombic crystal variants with an orthorhombic HZO[001] axis tilted by about 24°, 66° and 90° with respect to the plane-normal direction of the film. Electrical measurements confirm ferroelectricity, with a remanent polarization (P_r) of about 14 μC cm^{-2}, an endurance of up to 10^8 cycles and a retention of more than 10 years.

2. Experimental

HZO and LSMO films were grown in a single process on (111)-oriented $SrTiO_3$ (STO) substrates by pulsed laser deposition (KrF laser, 248 nm wavelength). The thicknesses of the HZO and LSMO films were around 6 and 22 nm, respectively. The HZO film was around 6 nm thick, which is the optimal thickness for high polarization in epitaxial films on (001)-oriented STO substrates.[20] The LSMO bottom electrode with a thickness of 22 nm combines high conductivity and flat surface (a LSMO electrode cannot be very thin because a dead layer at

Institut de Ciència de Materials de Barcelona (ICMAB-CSIC), Campus UAB, Bellaterra 08193, Barcelona, Spain. E-mail: ifina@icmab.es, fsanchez@icmab.es

† Electronic supplementary information (ESI) available: Projected cation structures of o-HZO crystallites and LSMO. Cation distance and angle in the three families of orthorhombic crystallites. Semicoherent interface along the [01$\bar{1}$]LSMO direction. Polarization loop measured by PUND. See DOI: https://doi.org/10.1039/d2tc00996j

‡ These authors contributed equally to this work.

the interface with STO reduces the conductance, but the surface roughness increases with thickness).[21] The deposition parameters of LSMO were a laser frequency of 5 Hz, an oxygen pressure of 0.1 mbar and a substrate temperature of 700 °C. The corresponding deposition parameters of HZO were 2 Hz, 800 °C and 0.1 mbar.[20,22] At the end of the deposition, the oxygen pressure was increased to 0.2 mbar and the heater was switched off. Platinum circular top electrodes (diameter 20 μm and thickness 20 nm) were deposited *ex situ* at room temperature by sputtering through stencil masks.

Crystal characterization was performed by X-ray diffraction (XRD) with Cu Kα radiation using a Siemens D5000 diffractometer equipped with a point detector, and a Bruker D8-Advance diffractometer equipped with a 2D detector. The identification of the crystal phase and the orientation in the individual HZO grains was performed by scanning transmission electron microscopy (STEM), using a JEOL ARM 200CF STEM with a cold field emission source, equipped with a CEOS aberration corrector and operated at 200 kV; cross-sectional high-angle annular dark field (HAADF) images were acquired. Film topography was analyzed by atomic force microscopy (AFM) using a Keysight 5100 scanning probe microscope. The ferroelectric characterization was performed using an AixACCT TFAnalyser2000 platform. Polarization loops were measured at 1 kHz by the dynamic leakage current compensation (DLCC) procedure[23] at room temperature in a top-bottom configuration, with the bottom LSMO electrode grounded. In addition, residual leakage subtraction was performed using reported equations.[24] Endurance was measured at room temperature cycling the sample at a frequency of 100 kHz using bipolar square pulses of the indicated amplitude and measuring polarization loops at 1 kHz. Retention was measured at 85 °C by poling the sample by a triangular pulse of 0.25 ms and determining the remanent polarization from the first polarization curve of the polarization loop measured at 1 kHz using the positive up negative down protocol after a delay time.

3. Results

In Fig. 1a, an XRD θ–2θ scan is shown. There are LSMO(111) and STO(111) diffraction peaks at 2θ around 40°, but no HZO reflections are observed. Wider regions of the reciprocal space were explored using a 2D detector. Fig. 1b shows a ψ–2θ map obtained by summing single ψ–2θ maps recorded at $\phi = 90 \pm 4°$, with an interval of $\Delta\phi = 1°$. Besides the STO(011) peak at $2\theta = 32.3°$ and $\psi = 35.3°$, two weaker spots belonging to orthorhombic HZO can be identified in Fig. 1b. They correspond to HZO(111) ($2\theta \sim 30.0°$, $\psi \sim 40.0°$) and HZO(002) ($2\theta \sim 34.8°$, $\psi \sim 24.8°$) reflections. Reflections corresponding to the monoclinic phase of HZO are not detected due to the limited sensitivity of the laboratory diffractometer. STEM characterization (shown below) reveals the presence of monoclinic crystallites. The pole figures from orthorhombic HZO(111) and HZO(002) reflections and the corresponding integrated ϕ scans are shown in Fig. 1c-1d and Fig. 1e (the panel at the right is a zoom of the region around $\phi = 115°$), respectively. There are three STO(011) substrate reflections, 120° apart with each other. HZO(002) reflections are found at the same ϕ position as the substrate peaks, while each HZO(111) reflection is split in two peaks at about 5° apart (Fig. 1e). Analysis of the pole figures points to the orientation of the HZO film close to (012). Considering a cell (for simplicity cubic) with the out-of-plane HZO(012) orientation, the corresponding HZO(002) planes are at $\psi = 26°$ and $\phi = 0°$, while HZO(111) planes are at $\psi = 39°$ and $\phi = \pm 114°$, leading to a ϕ splitting of HZO(111) of around $\pm 6°$. The broad peaks observed for HZO(111) and HZO(002) point to a certain mosaicity both the in-plane and out-of-plane. Nevertheless, the observed peaks are compatible with the existence of 3 distinct crystal domains with an epitaxial relationship $[0\bar{2}1]$HZO(012)//$[\bar{2}11]$STO(111). Due to the very low intensity of HZO(012) reflections and the nanometric thickness of the HZO film (6 nm), no HZO diffraction peaks are detected in the symmetric XRD scan (Fig. 1a).

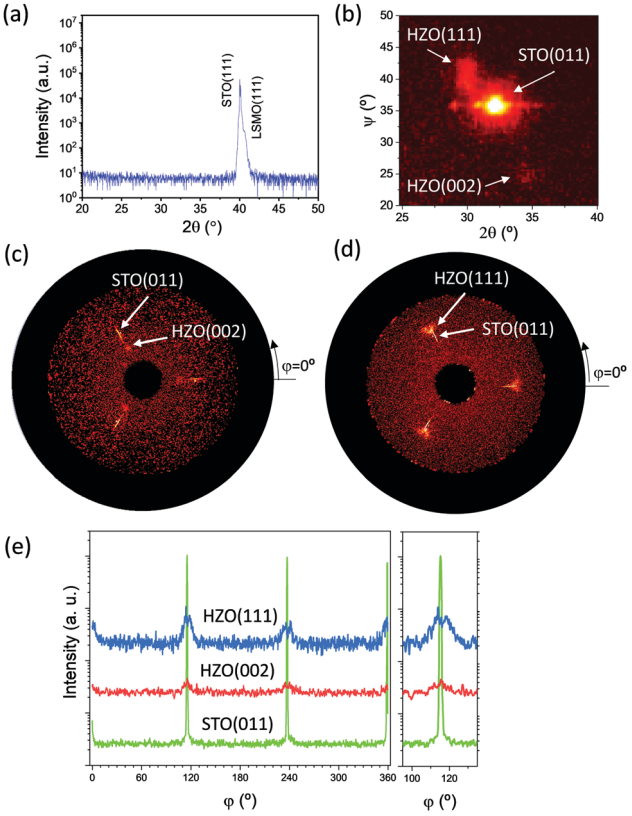

Fig. 1 (a) Symmetric $\theta/2\theta$ XRD scan measured using a 1D detector. (b) 2θ–ψ map around the asymmetric STO(011), orthorhombic HZO(111) and orthorhombic HZO(002) reflections. The map is a summing intensity of a set of maps measured using a 2D detector and recorded in a range of $\phi = \pm 4°$, with $\Delta\phi = 1°$. (c and d) Pole figures around the HZO(002) and (d) HZO(111) diffraction spots. The corresponding phi scans are plotted in (e) with the region around $\phi = 115°$ magnified. The intensity scale is logarithmic.

The topographic AFM image of a 5 μm × 5 μm region (Fig. 2a) shows that the surface of the film is very flat, with a root mean square roughness of 0.17 nm. The maximum height

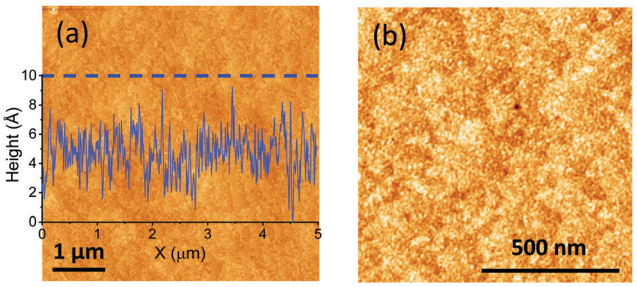

Fig. 2 (a) Topographic AFM image of the 5 μm × 5 μm scanned region, with a height profile along the horizontal dashed line. (b) Topographic AFM image of the 1 μm × 1 μm scanned region.

variation in the profile across the marked dashed blue line is less than 1 nm. The detailed view of Fig. 2a reveals the morphology of terraces and steps, which can also be appreciated in the zoomed 1 μm × 1 μm region (Fig. 2b).

The sample was inspected by STEM in order to obtain local information about the phase stabilization, epitaxy and microstructure. Fig. 3 shows cross-sectional HAADF images, observed along the [01$\bar{1}$] zone axis (corresponding to the [111]/[$\bar{2}$11] observation plane). Given the 3-fold symmetry of the LSMO/STO(111) surface planes, HZO epitaxial crystallites have the same probability of growing along the three equivalent in-plane directions (120° apart). The latter, given the epitaxial relationship between HZO and LSMO/STO(111), entails that only 1/3 of the crystallites can be observed simultaneously by STEM, while the other 2/3 of grains will be off-axis (Fig. S1, ESI†). This is compatible with the observations shown in Fig. 3a: those crystallites belonging to the 1/3 group are appropriately oriented

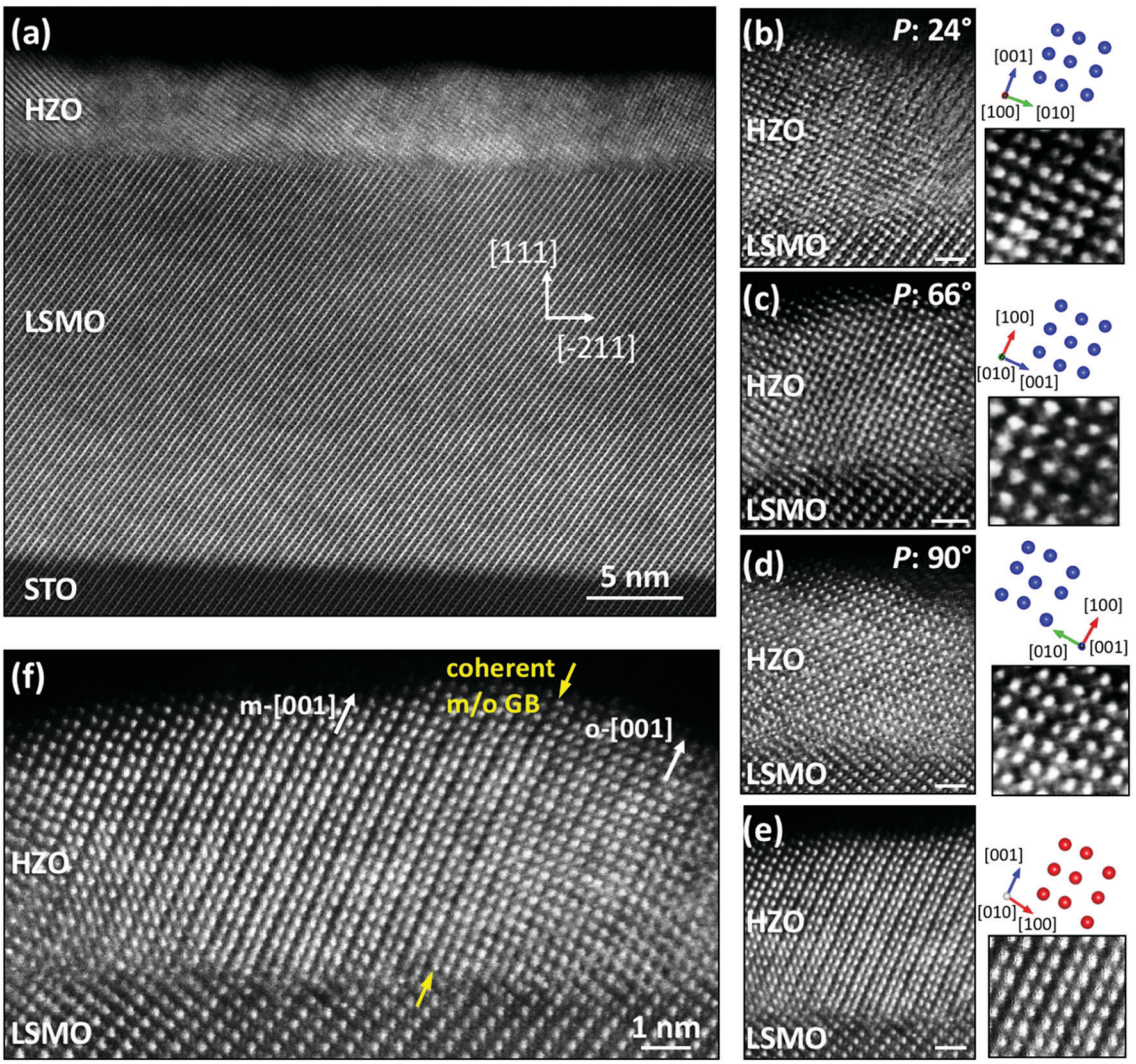

Fig. 3 (a) Large field of view HAADF image showing the STO(111) substrate, the LSMO(111) electrode and the HZO film. (b–d) Zooms of the three o-HZO crystal variants found in the HZO film, extracted from larger images collected at different locations. The [001] polar axis is tilted with respect to the plane-normal direction by 24° (b), 66° (c) and 90° (d). The *Pca2$_1$* orthorhombic model shows the Hf/Zr cations (blue balls) as seen along the different directions. (e) Zoom of the m-HZO phase and comparison with the *P2$_1$/c* monoclinic model showing the Hf/Zr cations (red balls). Note that the angle between the [001] and [100] directions is more than 90°, which is the characteristic of the monoclinic phase. (f) Zoom around the HZO film, showing tilted m-HZO(001) and o-HZO(001) grains and the coherent grain boundary (GB) between them, as indicated by the yellow top and bottom arrows. Scale bar in (b–e): 1 nm.

for the STEM observation and show well-defined cation atomic columns, which allows the epitaxial relationship between the orthorhombic HZO crystallites and LSMO/STO(111) to be identified. On the other hand, those crystallites belonging to the other crystal variants are not appropriately oriented for the STEM observation and the atomic column resolution is lost; instead, atomic planes are resolved. Three different atomic-column cation patterns can be discerned in the well-oriented orthorhombic HZO crystallites, with projection onto planes *b*–*c*, *a*–*c* and *a*–*b* (Fig. 3b–d). These cation patterns show features that reproduce the expected from the o-phase ($Pca2_1$) model (Fig. S2, ESI†). In every case, the orthorhombic HZO unit cell is found oriented with one ⟨001⟩ direction tilted by about 24° with respect to the out-of-plane direction, while the other directions have angles of about 66° and 90°. Note that these three variants are equivalent in a cubic, non-polar cell, but for an orthorhombic cell, the polar axis *c* has a different orientation in each of them. The similarity of the three orthorhombic lattice parameters (a = 5.234 Å, b = 5.010 Å, and c = 5.043 Å)[25] may allow the coexistence of these three crystal variants, each associated with a specific orientation of the polar *c* axis. Specifically, *c* is observed to lay at 24° (biggest out-of-plane polarization component, Fig. 3b), 66° (intermediate polarization component, Fig. 3c) or in the plane (90°, null out-of-plane polarization component, Fig. 3d) with respect to the plane-normal direction in three different grains. Therefore, each kind of grain is expected to contribute differently to the macroscopic polarization measured in the capacitor-like devices.

In addition to the polar tilted orthorhombic HZO(001), the non-polar monoclinic phase is also observed. Like the orthorhombic phase, the monoclinic phase presents the [001] direction tilted by about 24° away from the plane-normal direction. A zoomed monoclinic grain and comparison with model is shown in Fig. 3e. Interestingly, the coexistence of the orthorhombic (o) and monoclinic (m) crystallites with a similar epitaxial orientation allows the formation of coherent o/m grain boundaries (Fig. 3f), in contrast to the incoherent o(111)/m(001) grain boundaries found in HZO films on (001) substrates. In particular, the coherent m/o boundary forms despite the nominal 5% larger m(001) lattice spacing compared to the o(001) lattice spacing. The coherent boundaries are observed between grains with equivalent in-plane epitaxial orientation, but HZO crystallites can grow along any of the three equivalent in-plane directions. Thus, the grain boundaries between differently in-plane oriented HZO crystallites may not be coherent. This possibility could not be confirmed due to the difficulties in observing the cation columns for the misoriented crystallites. Besides, the intensity of the HAADF image (which scales approximately as Z^2, Z being the atomic number) at the HZO/LSMO interface (Fig. 3f) suggests a similar interfacial reconstruction to the one found in HZO/LSMO/STO(001),[26] where Hf/Zr atoms substitute Mn atoms right at the interface.

Grains that have grown along the two other equivalent in-plane directions of STO(111) and are not in perfect on-axis in the STEM images also provide valuable information. The resolved planes can be identified as belonging to the {111} or {$\bar{1}$11} families, which is the expected view if one grain is rotated in-plane by 120° clock or anticlockwise. The atomic columns remain unresolved in these grains due to an additional misorientation to 120° of about 6° (Fig. S1, ESI†). Interestingly, it can be seen that these {111} or {$\bar{1}$11} planes appear fully

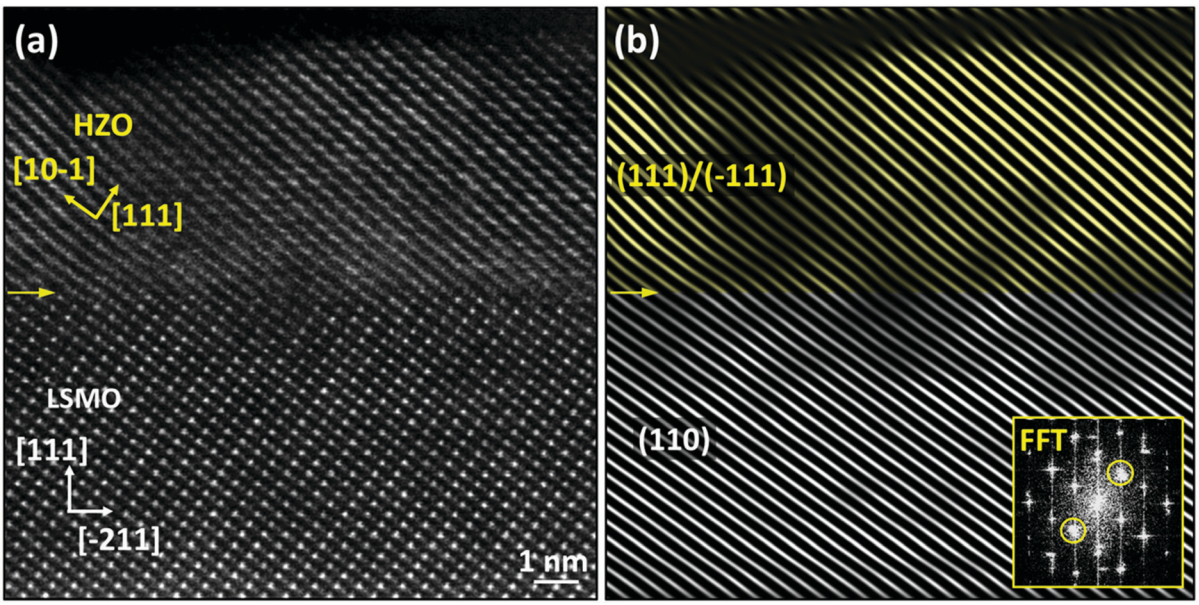

Fig. 4 (a) HAADF cross-sectional image of an orthorhombic HZO crystallite and the LSMO electrode. (b) The corresponding fast Fourier Transform (FFT) filtered image. {111}/{$\bar{1}$11} HZO planes and {110} LSMO planes are selected in the FFT (see the bottom-right inset) and used to obtain the image containing only the selected planes. Note that both HZO {111}/{$\bar{1}$11} and LSMO {110} reflections appear as one spot as they are not resolved separately. For clarity, planes in the HZO are shown in yellow while those in LSMO are shown in white. The location of the HZO/LSMO interface is indicated with a horizontal yellow arrow both in (a) and (b).

coherent with the (110) planes of LSMO, with a one-to-one matching along the direction parallel to the interface (corresponding to the following directions: $[42\bar{1}]$HZO/$[\bar{2}11]$LSMO, see Fig. 4a and b). On the other hand, the HZO/LSMO interface are semicoherent as seen along the $[01\bar{1}]$ LSMO zone axis as shown in Fig. S3 (ESI†). Given the dissimilarity between the HZO polymorphs and the LSMO structure, these well-matched planes can play an important role in the epitaxial stabilization of orthorhombic HZO on LSMO(111). The expected lattice mismatch between HZO $\{111\}$ or $\{\bar{1}11\}$ and LSMO/STO (110) planes is about 6%, which is a high but still feasible value for the strained growth of the nanometric film.

The current–electric field curve (Fig. 5a, red line) shows two clear ferroelectric switching current peaks. The corresponding polarization loop (blue line) evidences the ferroelectric behavior of the Pt/HZO/LSMO/STO(111) capacitor, with a remanent polarization P_r of above 14 μC cm^{-2}. A similar value has been obtained using the positive-up negative-down (PUND) method (Fig. S4, ESI†). The three families of orthorhombic crystallites have the c-axis tilted at 24°, 66° and 90° with respect to the normal, and thus their relative contribution to the measured polarization is different. The corresponding components of the polarization along the normal are $0.91P_{bulk}$, $0.41P_{bulk}$ and 0, where P_{bulk} is the polarization of HZO, which was calculated to be around 52–55 μC cm^{-2}.[27,28] The polarization of the film is expected to be $P = \alpha\cdot(1/3 \times 0.91P_{bulk} + 1/3 \times 0.41P_{bulk} + 0)$, where α is the fraction of the orthorhombic phase in the film. From the measurement of $P_r \sim 14$ μC cm^{-2}, it can be estimated that α is ~0.6, which qualitatively matches with the STEM observation. Fig. 5a also shows that the loop is notably shifted towards the negative electric field. The positive and negative coercive fields are $E_{C-} = -3.3$ MV cm^{-1} and $E_{C+} = 1.8$ MV cm^{-1}, respectively, signaling an imprint field of 750 kV cm^{-1} pointing towards the bottom LSMO electrode. The leakage current is plotted as a function of the electric field in Fig. 5b. The leakage is low, around 6×10^{-8} A cm^{-2} at 1 MV cm^{-1}. Fig. 5c shows the endurance measured applying bipolar cycles of amplitudes of 3 V (solid triangles) and 3.5 V (solid squares). There is not wake-up effect, despite the significant internal field in the pristine state (Fig. 5a). The initial polarization window at 3 V, 9.5 μC cm^{-2}, decreases slightly to 8.9 μC cm^{-2} after 10^3 cycles but degrades more severely with further cycling down to 2.5 μC cm^{-2} after 10^8 cycles. In the endurance measurement at 3.5 V, the higher initial polarization ($2P_r \sim 14$ μC cm^{-2}) decreased progressively to 8.8 μC cm^{-2} after 10^6 cycles, and then diminished faster up to 3.5 μC cm^{-2} after 10^8 cycles. The evolution of the leakage current during the endurance measurements (open symbols in Fig. 5c) does not reveal the correlation between ferroelectric fatigue and leakage. The lack of the correlation suggests that the fatigue process, to a great

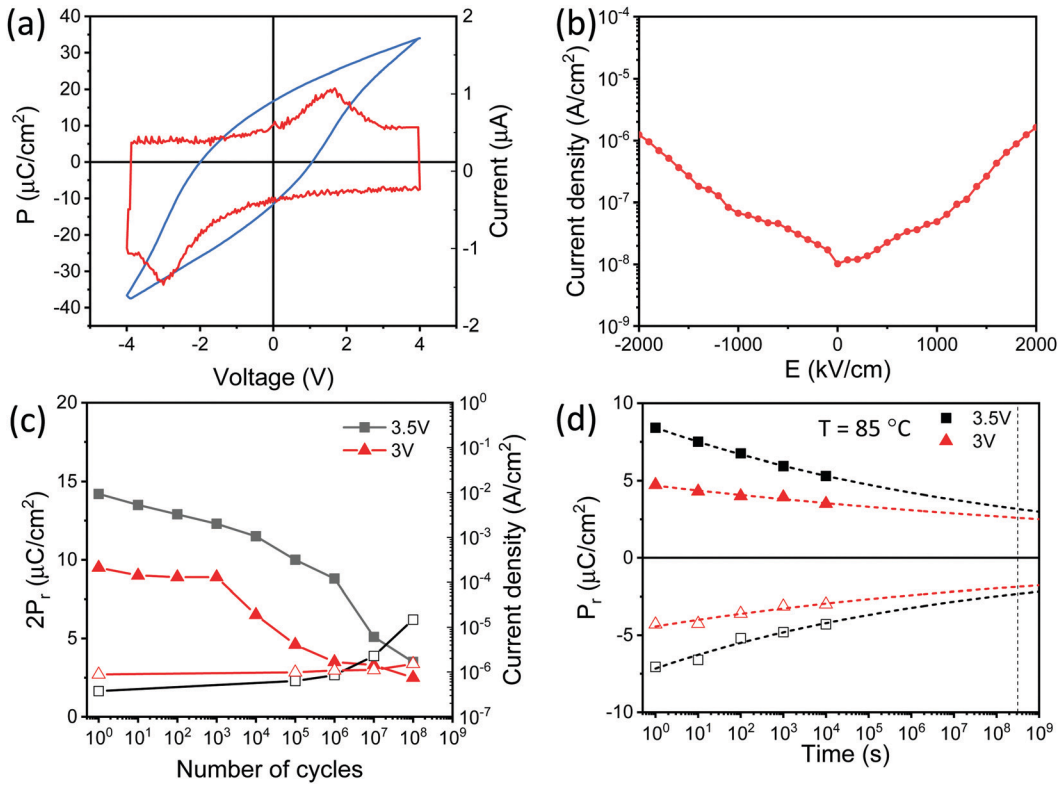

Fig. 5 (a) Current–electric field curve (red line) and the resultant ferroelectric polarization loop (blue line). (b) Leakage current as a function of the electric field. (c) Evolution of polarization ($2P_r$) with the number of bipolar cycles of amplitude 3 V (solid triangles) and 3.5 V (solid squares). Open symbols: evolution of the leakage current (value at 1V) during the endurance measurements at 3 V (triangles) and 3.5 V (squares). (d) Ferroelectric retention at 85 °C after poling with positive (solid symbols) or negative (open symbols) voltage pulses of 3.5 V (squares) and 3 V (triangles). Dashed lines correspond to $P_r \propto t_d^{-n}$ equation data fitting, where t_d refers to the time after poling. The vertical line marks a time of 10 years.

extent, is not originated by the formation of new oxygen vacancies. A similar behavior was observed in the epitaxial HZO films on LSMO/STO(001)[15] and buffered Si(001),[29] and it was proposed that fatigue in these epitaxial films is mainly caused by the fast growth of pinned ferroelectric domains within each orthorhombic grain.[30] The polarization retention was measured at 85 °C, poling the capacitors at the same voltage used for the endurance measurements (Fig. 5d). Triangles and squares correspond to the polarization retention after poling at 3 V and 3.5 V, respectively, and the measurements were done for positive poling (solid symbols) and negative (empty symbols) poling. The experimental data, up to 10^4 s, were fitted to the $P_r = P_0\, t_d^{-k}$ equation (dashed lines in Fig. 5d), being t_d the time after poling. The extrapolated retention extends beyond 10 years (vertical dotted line) for both poling voltages.

Conclusions

In conclusion, the epitaxial stabilization of orthorhombic HZO on LSMO/STO(111) has been demonstrated. In contrast to equivalent films on STO(001), HZO films are not (111)-oriented. They show tilted epitaxy and have three crystal variants with a polar [001] axis at different angles with respect to the plane-normal direction. The experimental ferroelectric polarization, about 14 μC cm^{-2}, matches well with the estimated value considering the crystal orientation of orthorhombic grains. Good retention and endurance are also demonstrated. The different crystal orientations compared with films on LSMO/STO(001) can be useful to investigate its impact on the ferroelectric properties. HZO on STO(111), with three crystal variants with a perfectly defined orientation, is suitable for the parallel functional characterization of monocrystalline grains with three specific orientations using piezoresponse force microscopy or in-situ transmission electron microscopy.

Conflicts of interest

There are no conflicts to declare.

Acknowledgements

Financial support from the Spanish Ministry of Science and Innovation (MCIN/AEI/10.13039/501100011033), through the Severo Ochoa FUNFUTURE (CEX2019-000917-S), PID2020-112548RB-I00 and PID2019-107727RB-I00 projects, the CSIC through the i-LINK (LINKA20338) program, and the Generalitat de Catalunya (2017 SGR 1377) is acknowledged. The project supported by a 2020 Leonardo Grant for Researchers and Cultural Creators, BBVA Foundation. IF acknowledges Ramón y Cajal contract RYC-2017-22531. TS is financially supported by the China Scholarship Council (CSC) with No. 201807000104. TS work has been done as a part of his PhD program in Materials Science at Universitat Autònoma de Barcelona. SE acknowledges the Spanish Ministry of Science and Innovation for his PhD contract (SEV-2015-0496-16-3) and its cofunding by the ESF. ICTS-CNME at UCM is acknowledged for offering access to STEM microscopy and expertise.

References

1 T. S. Böscke, J. Müller, D. Bräuhaus, U. Schröder and U. Böttger, *Appl. Phys. Lett.*, 2011, **99**, 102903.
2 S. Yu, J. Hur, Y. C. Luo, W. Shim, G. Choe and P. Wang, *Semicond. Sci. Technol.*, 2021, **36**, 104001.
3 J. Y. Kim, M. J. Choi and H. W. Jang, *APL Mater.*, 2021, 9.
4 J. Y. Park, K. Yang, D. H. Lee, S. H. Kim, Y. Lee, P. R.-S. Reddy, J. L. Jones and M. H. Park, *J. Appl. Phys.*, 2020, **128**, 240904.
5 M. H. Park, Y. H. Lee, T. Mikolajick, U. Schroeder and C. S. Hwang, *MRS Commun.*, 2018, **8**, 795.
6 T. Mikolajick, S. Slesazeck, M. H. Park and U. Schroeder, *MRS Bull.*, 2018, **43**, 340.
7 U. Schröder, C. S. Hwang and H. Funakubo, *Ferroelectricity in Doped Hafnium Oxide: Materials, Properties and Devices*, Woodhead Publishing, 2019.
8 M. H. Park, Y. H. Lee, H. J. Kim, Y. J. Kim, T. Moon, K. Do Kim, J. Müller, A. Kersch, U. Schroeder, T. Mikolajick and C. S. Hwang, *Adv. Mater.*, 2015, **27**, 1811.
9 T. Shimizu, K. Katayama, T. Kiguchi, A. Akama, T. J. Konno, O. Sakata and H. Funakubo, *Sci. Rep.*, 2016, **6**, 32931.
10 H. Y. Yoong, H. Wu, J. Zhao, H. Wang, R. Guo, J. Xiao, B. Zhang, P. Yang, S. J. Pennycook, N. Deng, X. Yan and J. Chen, *Adv. Funct. Mater.*, 2018, **28**, 1.
11 J. Lyu, I. Fina, R. Solanas, J. Fontcuberta and F. Sánchez, *Appl. Phys. Lett.*, 2018, **113**, 082902.
12 Y. Wei, P. Nukala, M. Salverda, S. Matzen, H. J. Zhao, J. Momand, A. S. Everhardt, G. Agnus, G. R. Blake, P. Lecoeur, B. J. Kooi, J. Íñiguez, B. Dkhil and B. Noheda, *Nat. Mater.*, 2018, **17**, 1095.
13 I. Fina and F. Sánchez, *ACS Appl. Electron. Mater.*, 2021, **3**, 1530.
14 J. Lyu, T. Song, I. Fina and F. Sánchez, *Nanoscale*, 2020, **12**, 11280.
15 T. Song, R. Bachelet, G. Saint-Girons, R. Solanas, I. Fina and F. Sánchez, *ACS Appl. Electron. Mater.*, 2020, **2**, 3221.
16 M. Cervo Sulzbach, H. Tan, S. Estandía, J. Gàzquez, F. Sánchez, I. Fina and J. Fontcuberta, *ACS Appl. Electron. Mater.*, 2021, **3**, 3657.
17 S. Estandía, J. Gàzquez, M. Varela, N. Dix, M. Qian, R. Solanas, I. Fina and F. Sánchez, *J. Mater. Chem. C*, 2021, **9**, 3486.
18 P. Jiao, J. Li, Z. Xi, X. Zhang, J. Wang, Y. Yang, Y. Deng and D. Wu, *Appl. Phys. Lett.*, 2021, **119**, 252901.
19 T. Song, H. Tan, S. Estandía, J. Gàzquez, M. Gich, N. Dix, I. Fina and F. Sánchez, *Nanoscale*, 2022, **14**, 2337.
20 J. Lyu, I. Fina, R. Solanas, J. Fontcuberta and F. Sánchez, *ACS Appl. Electron. Mater.*, 2019, **1**, 220.
21 M. Huijben, L. W. Martin, Y.-H. Chu, M. B. Holcomb, P. Yu, G. Rijnders, D. H.-A. Blank and R. Ramesh, *Phys. Rev. B: Condens. Matter Mater. Phys.*, 2008, **78**, 094413.

22 J. Lyu, I. Fina and F. Sánchez, *Appl. Phys. Lett.*, 2020, **117**, 072901.
23 R. Meyer, R. Waser, K. Prume, T. Schmitz and S. Tiedke, *Appl. Phys. Lett.*, 2005, **86**, 142907.
24 S. González-Casal, I. Fina, F. Sánchez and J. Fontcuberta, *ACS Appl. Electron. Mater.*, 2019, **1**, 1937.
25 L. L. Tao, T. R. Paudel, A. A. Kovalev and E. Y. Tsymbal, *Phys. Rev. B*, 2017, **95**, 1.
26 S. Estandía, T. Cao, R. Mishra, I. Fina, F. Sánchez and J. Gazquez, *Phys. Rev. Mater.*, 2021, **5**, 1.
27 T. D. Huan, V. Sharma, G. A. Rossetti and R. Ramprasad, *Phys. Rev. B: Condens. Matter Mater. Phys.*, 2014, **90** 064111.
28 F. Delodovici, P. Barone and S. Picozzi, *Phys. Rev. Mater.*, 2021, **5**, 064405.
29 J. Lyu, I. Fina, J. Fontcuberta and F. Sánchez, *ACS Appl. Mater. Interfaces*, 2019, **11**, 6224.
30 T. Song, S. Estandía, H. Tan, N. Dix, J. Gàzquez, I. Fina and F. Sánchez, *Adv. Electron. Mater.*, 2021, 2100420.